Curvelet-based seismoelectric data processing

Sheldon Warden, Stéphane Garambois, Pascal Sailhac, Laurence Jouniaux, Maksim Bano

HAL Id: hal-00724796
https://hal.science/hal-00724796

Curvelet-based seismoelectric data processing

S. Warden,[1] S. Garambois,[2] P. Sailhac,[1] L. Jouniaux[1] and M. Bano[1]

[1]*Institut de Physique du Globe de Strasbourg, CNRS UMR 7516, Université de Strasbourg, Strasbourg, France. E-mail: sheldon.warden@etu.unistra.fr*
[2]*Isterre, Université Joseph Fourier, CNRS UMR 5275, Grenoble, France*

SUMMARY

Seismoelectromagnetic conversions are induced through electrokinetic phenomena occurring when passing seismic waves induce relative fluid to solid displacements. Information on porous material properties provided by the type I coseismic electric field accompanying surface and body waves is limited to the vicinity of the electrical receivers, as opposed to the type II electromagnetic interface response (IR) which can help detect porous contrasts and/or fluid changes within the subsurface 'at depth'. For general field geometries, the problem is that type II disturbances exhibit lower amplitudes than type I fields and are difficult to access directly. Hence, separating both types of waves is a critical step when processing seismoelectric data. Synthetic seismograms and electrograms, generated with a full-waveform seismoelectric forward modelling code written by Garambois & Dietrich, enabled us to study the behaviour of the IR's characteristic dipolar amplitude pattern recovered through filtering.

To better preserve the IR amplitudes, we have developed a new filtering strategy based on the Fast Discrete Curvelet Transform. Seismic or seismoelectric wave fronts can be optimally described using this multiscale decomposition over multidirectional anisotropic needle-shape structures. We have built a mask in the curvelet domain zeroing out seismoelectric samples corresponding to non-zero samples from the accelerogram, thus taking advantage of the relationship between seismic and seismoelectric waves for type I fields. This mask consists of a threshold function combined with a Gaussian distribution promoting horizontal (i.e. zero-slowness) directions. When applied to synthetic data, this filter enabled to successfully extract the IR although less altering its dipolar radiation pattern than the conventional dip-based techniques. This strategy was successfully applied to a seismoelectric data set acquired in sedimentary deposits, and permitted to isolate an IR generated at the water table.

Key words: Image processing; Wavelet transform; Electrical properties; Hydrogeophysics; Wave propagation; Acoustic properties.

1 INTRODUCTION

Electrokinetic phenomena arise from the relative motion between the rock matrix and the fluid within the rock pores (Jouniaux & Ishido 2012) and are at the origin of self-potential (Jouniaux *et al.* 2009), electroseismic (Thompson *et al.* 2007) and seismoelectric (Dupuis *et al.* 2007) observations, the latter being the main focus of this paper.

When a seismic wave propagates through a fluid-containing porous medium, it generates at least two types of signals. (1) It creates a relative movement between the medium's fluid and solid phases, which, because of the presence of an electric double layer at the grain-fluid boundary, sets in motion the free electric charges present in the pore fluid with respect to the charges adsorbed at the grain surface (Davis *et al.* 1978). The electric field associated with the resulting charge separation is contained within the seismic waves; as it travels at the same seismic velocity, it is known as the 'coseismic' electric field, or type I signal. (2) When a seismic

wave encounters a boundary between two media presenting different hydromechanical and/or electrical properties, the transient charge separation travelling within this wave is disturbed. The resulting imbalance acts as a secondary source which can be approximated as an electric dipole oscillating perpendicularly to the interface and centreed at the first seismic Fresnel zone (Thompson & Gist 1993; Garambois & Dietrich 2001). The radiated 'interface response' (IR) or type II signal (Dupuis *et al.* 2009) travels at the same velocity as electromagnetic (EM) waves in the medium, that is several orders of magnitude faster than the seismic waves, and is therefore observed almost simultaneously at all receivers.

These 'seismoelectric' conversions should be distinguished from their 'electroseismic' reciprocal counterparts, for which the coupling is triggered by the conduction of electric currents. Both types of phenomena have been studied on the field to investigate hydraulic reservoirs (Dupuis *et al.* 2007; Strahser 2007; Dupuis *et al.* 2009; Strahser *et al.* 2011), as well as hydrocarbon reservoirs (Thompson *et al.* 2005). It has been shown that not only the reservoir depth,

but also its geometry can be imaged using the amplitudes of the electroseismic signals (Thompson *et al.* 2007). The seismoelectric conversions have also been studied in laboratory (Zhu *et al.* 1999; Bordes *et al.* 2006, 2008) and the existence of the interfacial response has been evidenced by Block & Harris (2006) and Chen & Mu (2005).

Other studies have highlighted that seismoelectric conversions are appealing for the detection of subsurface interfaces induced by contrasts in electrical properties, permeability or porosity (Garambois & Dietrich 2002; Pain *et al.* 2005; Rosid & Kepic 2005; Schakel & Smeulders 2010; Schakel *et al.* 2011, 2012) and that seismoelectric imaging has the potential to resolve thin layers that are undetectable with other techniques (Pride & Garambois 2005). Borehole seismoelectrics may also help detect and characterize fractured zones: Mikhailov *et al.* (2000) were able to correlate fracture density logs with the amplitudes of the very weak electric field they measured (a few $\mu V\ m^{-1}$). Moreover, Hunt & Worthington (2000) showed a relationship between fracture aperture and the frequency content of the observed seismoelectric fields they acquired during electrokinetic borehole logging experiments. Hu & Gao (2011) also studied the EM field generated by a finite fault through electrokinetic conversions. Finally, seismoelectric conversions were also studied in the frame of earthquake seismology, as the seismoelectric waves generated by a double-couple source were investigated by Gao & Hu (2010).

As it does not exist outside the seismic disturbance, the coseismic wavefield only provides local information restricted to the vicinity of the dipole receivers: when these are deployed inside a borehole, the study of coseismic effects may provide valuable information about the medium's porosity and permeability near the borehole at depth (Dupuis & Butler 2006; Hu *et al.* 2007; Guan *et al.* 2012). However, when such configurations are not available, it becomes necessary to work with surface seismoelectric layouts (Fig. 1). In this case, coseismic waves are only sensitive to porous properties in the vicinity of the receivers, as opposed to interface dipolar responses, which allow to illuminate contrasts 'at depth'. Unfortunately, as for classical field geometries it is several orders of magnitude weaker than the coseismic waves, the interface signal needs to be extracted through wave separation techniques, without any distortion if waveforms

are to be inverted or if Amplitude-Versus-Offset analysis is to be performed.

Simple bandpass filtering may grant acceptable results in a few favourable scenarios (Garambois & Dietrich 2001), but most cases call for more refined methods. Several properties of the seismoelectric IR can be used to identify it and separate it from the coseismic wavefield: (1) its dipolar amplitude pattern, (2) its opposite polarities on either side of the shot point and (3) the EM velocity at which it travels, several orders of magnitude faster than seismic waves, which results in the IR appearing as a nearly horizontal arrival on the electrograms.

The contribution of the present paper is twofold. First, we take existing comparisons (Haines *et al.* 2007a) between seismoelectric data processing techniques one step further by discussing the impact of these previously reviewed methods, namely frequency-wavenumber ($f - k$) and Radon domain filtering, on IR amplitudes. For this purpose, we use a seismoelectromagnetic wave propagation modelling code based on a generalized reflectivity method (Garambois & Dietrich 2002). It permits to model IRs independently from the coseismic wavefield and compare these synthetic radiation patterns with those recovered through filtering.

Secondly, we introduce a new filtering strategy based on the curvelet transform, a 2-D wavelet transform combining useful properties from different processing techniques (Fadili & Starck 2009). The curvelet transform can indeed be seen as a series of $f - k$ transforms or multiscale Radon transforms. We notably examine how these multiscale and multidirectional wavelets help improve the type I/type II wave separation and if they affect the radiation pattern.

After introducing the seismoelectric background theory, we recall in the paper the main characteristics of the modelling code used throughout this study. We then apply the investigated processing techniques, namely $f - k$, Radon and curvelet filtering techniques to a set of synthetic seismoelectric data. We compare their performances in terms of amplitude preservation when White Gaussian Noise (WGN) is introduced and when the type I/type II amplitude ratio varies. Finally, we test all three methods on a seismoelectric data set acquired in sedimentary deposits.
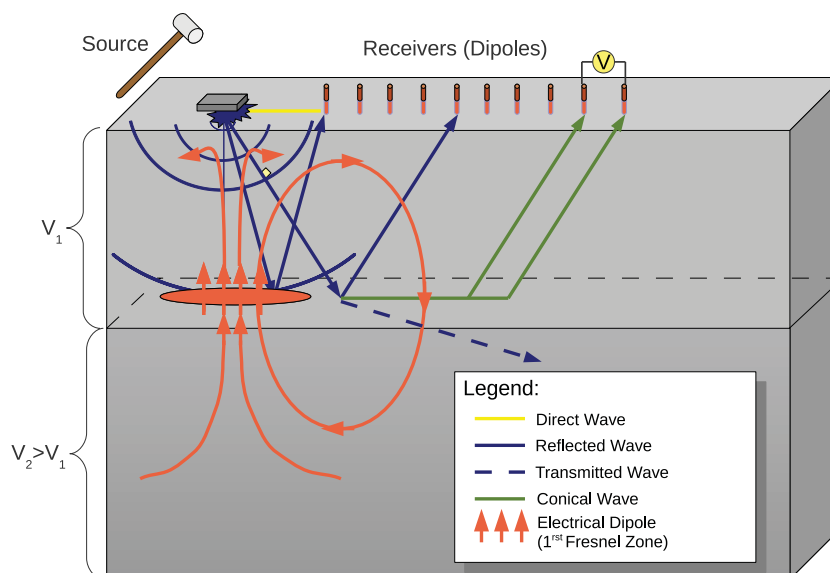

Figure 1. Typical seismoelectric layout used throughout this study.

2 SEISMOELECTRIC DATA MODELLING

We start with the set of equations governing the coupling between the mechanical and EM wavefields in porous media as derived by Pride (1994).

It combines the Maxwell equations, describing the EM wave propagation, with the Biot equations, describing the seismic wave propagation in a saturated porous medium via two transport relations, written here for a $e^{-i\omega t}$ time dependence:

$$\mathbf{J} = \sigma(\omega)\mathbf{E} + L(\omega)\left(-\nabla p + \omega^2 \rho_f \mathbf{u_s}\right), \tag{1}$$

$$-i\omega\mathbf{w} = L(\omega)\mathbf{E} + \frac{k(\omega)}{\eta}\left(-\nabla p + \omega^2 \rho_f \mathbf{u_s}\right). \tag{2}$$

In the first equation, the macroscopic electrical current density $\mathbf{J}$ is the sum of the average conduction and streaming current densities. The fluid–solid relative displacement $\mathbf{w}$ of the second equation is separated into electrically and mechanically induced contributions. The electrical fields and mechanical forces that create the current density $\mathbf{J}$ (eq. 1) and fluid–solid relative displacement $\mathbf{w}$ (eq. 2) are, respectively, $\mathbf{E}$ and $(-\nabla p + \omega^2 \rho_f \mathbf{u_s})$, where p is the pore fluid pressure, $\mathbf{u_s}$ is the solid displacement and $\mathbf{E}$ is the electric field.

The parameter $L(\omega)$ describing the coupling between the seismic and EM fields is complex and frequency-dependent (Pride 1994):

$$L(\omega) = L_0 \left[1 - i\frac{\omega}{\omega_c}\frac{m}{4}\left(1 - 2\frac{d}{\Lambda}\right)^2 \left(1 - i^{3/2} d\sqrt{\frac{\omega\rho_f}{\eta}}\right)^2 \right]^{-\frac{1}{2}}, \tag{3}$$

where L_0 is the low-frequency electrokinetic coupling, d is related to the Debye length, Λ is a porous material geometry term (Johnson *et al.* 1987) and m is a dimensionless number, detailed in Pride (1994). The other two coefficients, $\sigma(\omega)$ and $k(\omega)$, are the dynamic electric conductivity and permeability of the porous material, respectively.

Garambois & Dietrich (2001) derived the low-frequency coseismic transfer function valid at frequencies lower than the Biot's frequency (related to the angular frequency ω_c) separating viscous and inertial flows. In this case, and assuming the Biot's moduli $C \ll H$, they showed that the seismoelectric field $\mathbf{E}$ is proportional to the grain acceleration for *P* waves:

$$\mathbf{E} \simeq \frac{\epsilon_f \zeta}{\eta\sigma_f}\,\rho_f\ddot{\mathbf{u}}, \tag{4}$$

where σ_f, ϵ_f, η and ρ_f are, respectively, the fluid conductivity, fluid electric permittivity, dynamic viscosity and fluid density. Eq. (4) shows that transient seismoelectric magnitudes will be affected by the bulk density of the fluid and are inversely proportional to the fluid conductivity and viscosity and proportional to the zeta potential (which depends on the pH). One can rewrite eq. (4) in terms of streaming coefficient or seismoelectric coupling coefficient. The streaming coefficient C_s is described by the Helmholtz–Smoluchowski equation when the surface conductivity can be neglected with respect to the fluid bulk conductivity:

$$C_s = \frac{\epsilon_0 \kappa_f \zeta}{\eta\sigma_f}. \tag{5}$$

Eq. (240) in Pride (1994) gives the seismoelectric coupling coefficient:

$$L_0 = -\frac{\phi}{\alpha_\infty}\frac{\epsilon_0 \kappa_f \zeta}{\eta}\left(1 - 2\frac{\tilde{d}}{\Lambda}\right), \tag{6}$$

where ϕ is the porosity and α_∞ the tortuosity; $\tilde{d}$ is a length [m] defined as $\int_0^D \frac{\Phi_0(\chi)}{\zeta} d\chi$, where χ is a local coordinate measuring the distance to the shear plane of the electrical double layer, $\Phi_0(\chi)$ the potential in the vicinity of this shear plane and D a multiple of the Debye length. Λ is the hydraulic radius [m]. When surface conductivity is not taken into account, the rock conductivity can be expressed as $\sigma_r = \frac{\phi\sigma_f}{\alpha_\infty}$. Under low-frequency approximations one can write $\tilde{d} \ll \Lambda$, thus leading to:

$$\mathbf{E} \simeq -\frac{L_0}{\sigma_r}\,\rho_f\ddot{\mathbf{u}} = C_{sp}\rho_f\ddot{\mathbf{u}}. \tag{7}$$

The value of the streaming potential coefficient C_{sp} [V Pa^{-1}] can be inferred from studies on various rocks and sediments (Jouniaux *et al.* 1999; Hase *et al.* 2003; Tosha *et al.* 2003; Guichet *et al.* 2006; Jaafar *et al.* 2009; Allègre *et al.* 2010, 2012; Schoemaker *et al.* 2012). An alternative is to compute the ζ potential as a function of the electrolyte concentration C_0 [mol L^{-1}] from the empirical formula proposed by Pride & Morgan (1991), based on a compilation of measurements performed on quartz minerals saturated with NaCl and KCl electrolytes at pH = 7 and $T = 25\,^\circ$C:

$$\zeta = 8 + 26\log_{10} C_0, \tag{8}$$

with ζ in mV. As this equation is valid for molarities below 0.1 mol L^{-1}, it covers the concentration range of interest ($10^{-6} < C < 10^{-1}$ mol L^{-1}). We therefore use it to compute the ζ potential in the following model dealing with sand and sandstone. For example, a concentration of 10^{-2} mol L^{-1} yields a ζ potential of -44 mV, whereas $\zeta = -96$ mV for a concentration of 10^{-4} mol L^{-1}.

The semi-analytical seismoelectric modelling code used here combines the generalized reflectivity technique developed by Kennett & Kerry (1979) with the discrete wavenumber integration method (Bouchon & Aki 1977; Bouchon 1981). It accounts for the full set of macroscopic equations derived by Pride (1994) to describe the 3-D propagation of seismic and EM waves in stratified porous media in the frequency domain.

The formalism proposed by Kennett & Kerry (1979) allows to write the displacement, stress and EM fields as a function of three independent terms: a source term, a generalized reflectivity term and a term expressing the conversion between the potentials and the fields at the receivers. Multiple reflections can be ignored, as can be direct waves. Furthermore, specific coefficients in the reflection–transmission matrices computed at an interface can be artificially amplified or cancelled, which can help highlight IRs that would otherwise remain concealed by stronger arrivals. This feature is also useful when seeking to model the theoretical amplitude distribution of IRs independently from the coseismic wavefield.

In previous work by Haines *et al.* (2007b), data were modelled using a finite-difference approach (Haines & Pride 2006) which did not include a free surface and therefore did not permit to model Rayleigh waves. This limitation lead the authors to work with data created by adding synthetic IRs to seismoelectric field recordings. By taking the free surface into account, our approach allows to model Rayleigh waves, whose strong amplitudes usually have a dramatic impact on real seismoelectric records.

For the benchmark, we have modelled a simple tabular medium, consisting of a single 30-m-thick sand layer on top of a less porous, less permeable sandstone half-space. We have chosen to model strong permeability and salt concentration contrasts between these two fully saturated units (Table 1). The acquisition geometry consists of a seismic source with peak frequency $f_{\text{peak}} = 120$ Hz, located in the centre of a 100-m-long profile stretching between -50 and

Table 1. Physical properties describing the two-layers model used in this study, (1) sand and (2) sandstone. The ζ potential is calculated from C_0 (Pride & Morgan 1991). Seismic velocities V_{Pf} and V_S computed at peak frequency $f_{\text{peak}} = 120$ Hz are also given here.

	ϕ	k m^2	K_s Pa	K_f Pa	K_{fr} Pa	G_{fr} Pa	η Pa s	ρ_s kg m^{-3}	ρ_f kg m^{-3}	C_0 mol L^{-1}	V_{Pf} m s^{-1}	V_S m s^{-1}
1	0.35	10^{-11}	35×10^9	2.27×10^9	3×10^8	4×10^8	10^{-3}	2.6×10^3	10^3	10^{-4}	1789	443
2	0.20	10^{-13}	35×10^9	2.27×10^9	4×10^9	5×10^9	10^{-3}	2.6×10^3	10^3	10^{-2}	2812	1481

(a) Vertical displacement uz

(b) Horizontal displacement ux

(c) Electric field Ex
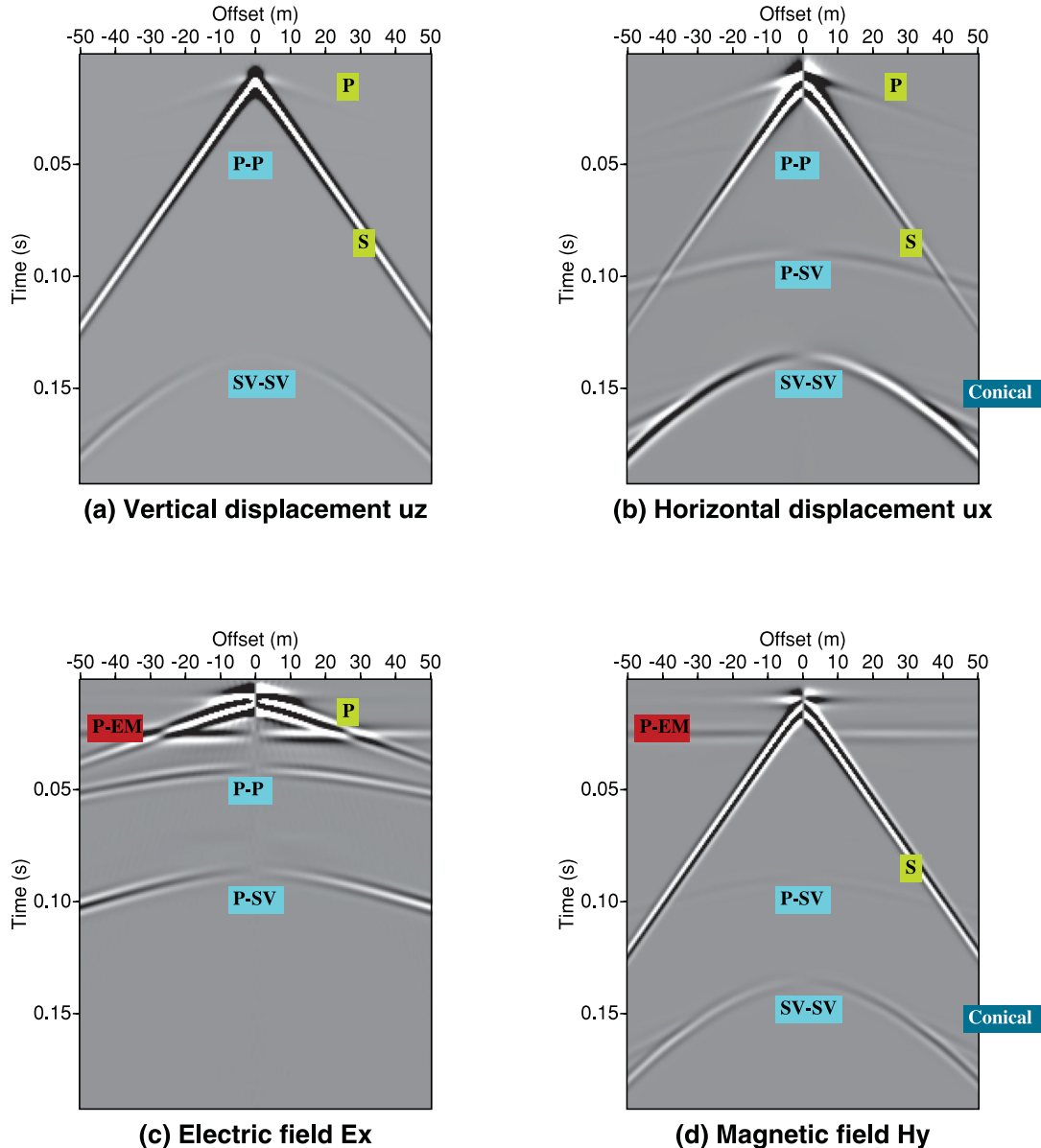
(d) Magnetic field Hy

Figure 2. Synthetic vertical (a) and horizontal (b) seismograms, electrogram (c) and magnetogram (d) created with our modelling code (Garambois & Dietrich 2001), using a vertical source buried at $z_s = 3$ m and 201 evenly spaced receivers located between offsets $x = -50$ m and $x = 50$ m. The model consists of a 30-m-thick sand layer on top of a sandstone half-space, with material properties as described in Table 1. The zero-move out P-EM interface response has been multiplied by 20. Free surface reflections were not taken into account.

50 m. The source wavelet modelled here is a Ricker ('mexican hat') wavelet. Two hundred one 1-m-long dipoles are evenly spaced along the profile, with 0.5 m between two consecutive receiver pairs. It was necessary to boost the P-EM conversion coefficients by 20 ito visualize the associated response (Fig. 2).

Both rocks are fully saturated, with the saturating fluid being more conductive in the underlying sandstone. To simulate the impact of

a sledgehammer on a plate, we have introduced a vertical force source with a momentum of 7.85×10^3 N s, which corresponds to a stack of a 100 shots acquired with a 7.85 kg sledgehammer impacting the ground at 10 m s^{-1}. The modelling program returns the vertical (u_z) and horizontal (u_x) displacements as well as the Transverse Magnetic (TM) EM field (E_x and H_y) (Haartsen & Pride 1997; Garambois & Dietrich 2002).
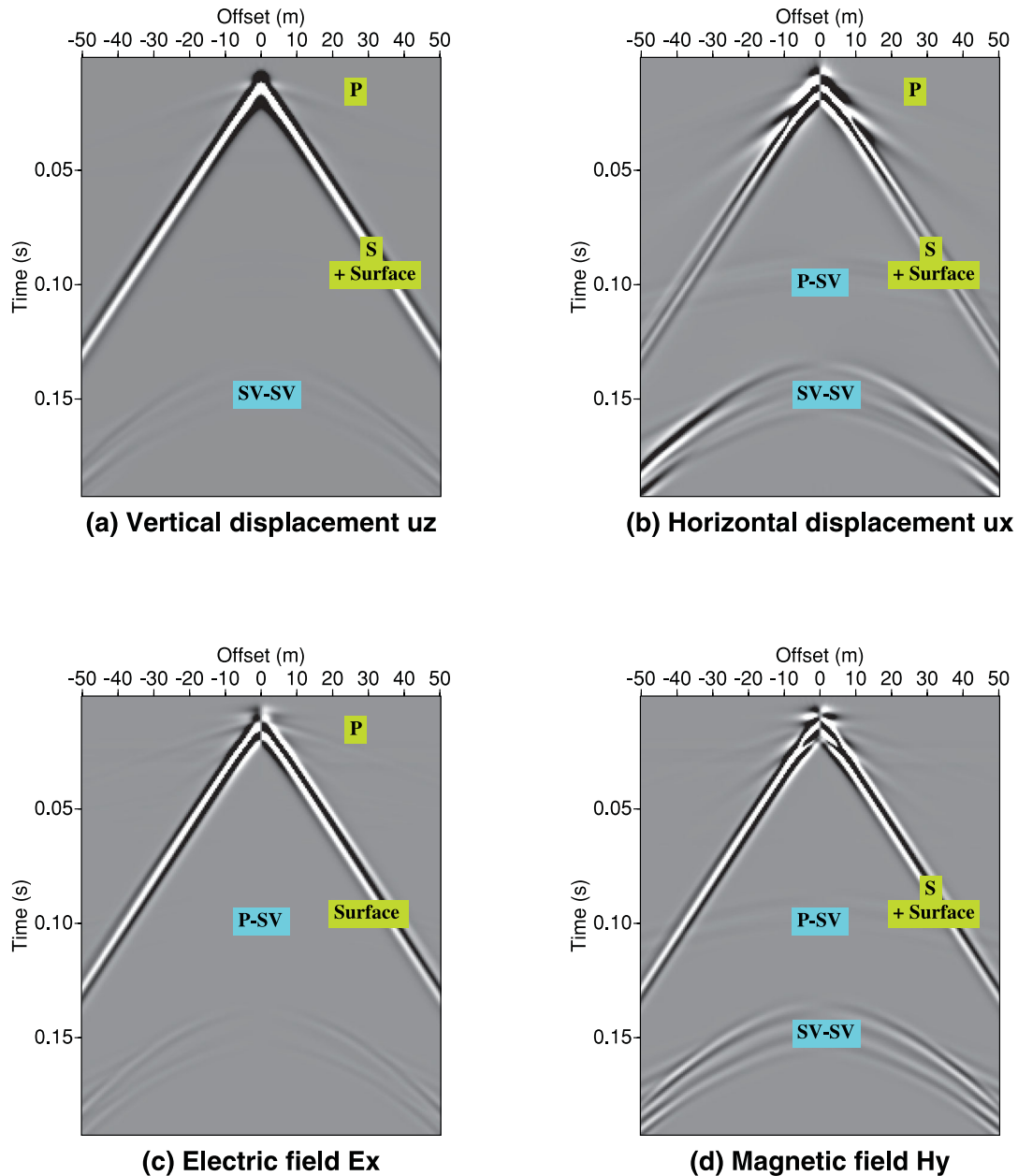
Figure 3. Synthetic recordings modelled as in Fig. 2, but with free surface reflections taken into account. Although still present, the interface response and the coseismic *P-SV* reflection hyperbola appear masked by the energetic surface waves. Conical waves are present as in Fig. 2, but we have chosen not to indicate them, as they are now interfering with multiple reflections.

Figs 2 and 3 show the synthetic seismograms, electrograms and magnetograms obtained for this set of parameters, without and with the free surface, respectively. One can identify the coseismic counterparts of the direct *P* wave and both the *P–P* and *P–SV* reflections, as well as the *P*-EM IR (Fig. 2c); here *SV* refers to the *S* waves polarized in the vertical plane. It can also be noted that the direct *S* wave does not generate any coseismic electric wave but a coseismic magnetic wave instead, as measured in the laboratory (Bordes *et al.* 2008). Fig. 3 was obtained by including free surface conditions into the computations and exhibit mainly Rayleigh waves and their electric and magnetic signature.

Fig. 4 displays the characteristic amplitude distribution for type I and type II seismoelectric conversion waves. The IR (Figs 4c and d) was modelled without the coseismic wavefield by multiplying the

P_f −TM, P_s −TM and *SV*-TM coefficients by 10^8 and afterwards by dividing the recovered amplitudes by this arbitrary factor. It can be seen that the IR displays a dipolar pattern, centred below the shot point, whereas the coseismic surface waves decay just like their seismic counterparts, at a rate proportional with the inverse of the square root of the distance. The maximum amplitude of the coseismic part is 1 mV whereas the one of the interfacial response is about 10^{-4} mV.

Modelling different data sets while allowing the 'type II/type I' ratio to vary is crucial, as it helps estimate how weak the IR can be with respect to the overlapping coseismic wavefield such that it can still be recovered through filtering. Before running this sensitivity study, we have applied all filtering methods to a sample record for which the ratio was set to 0.1 (a favourable case, for which
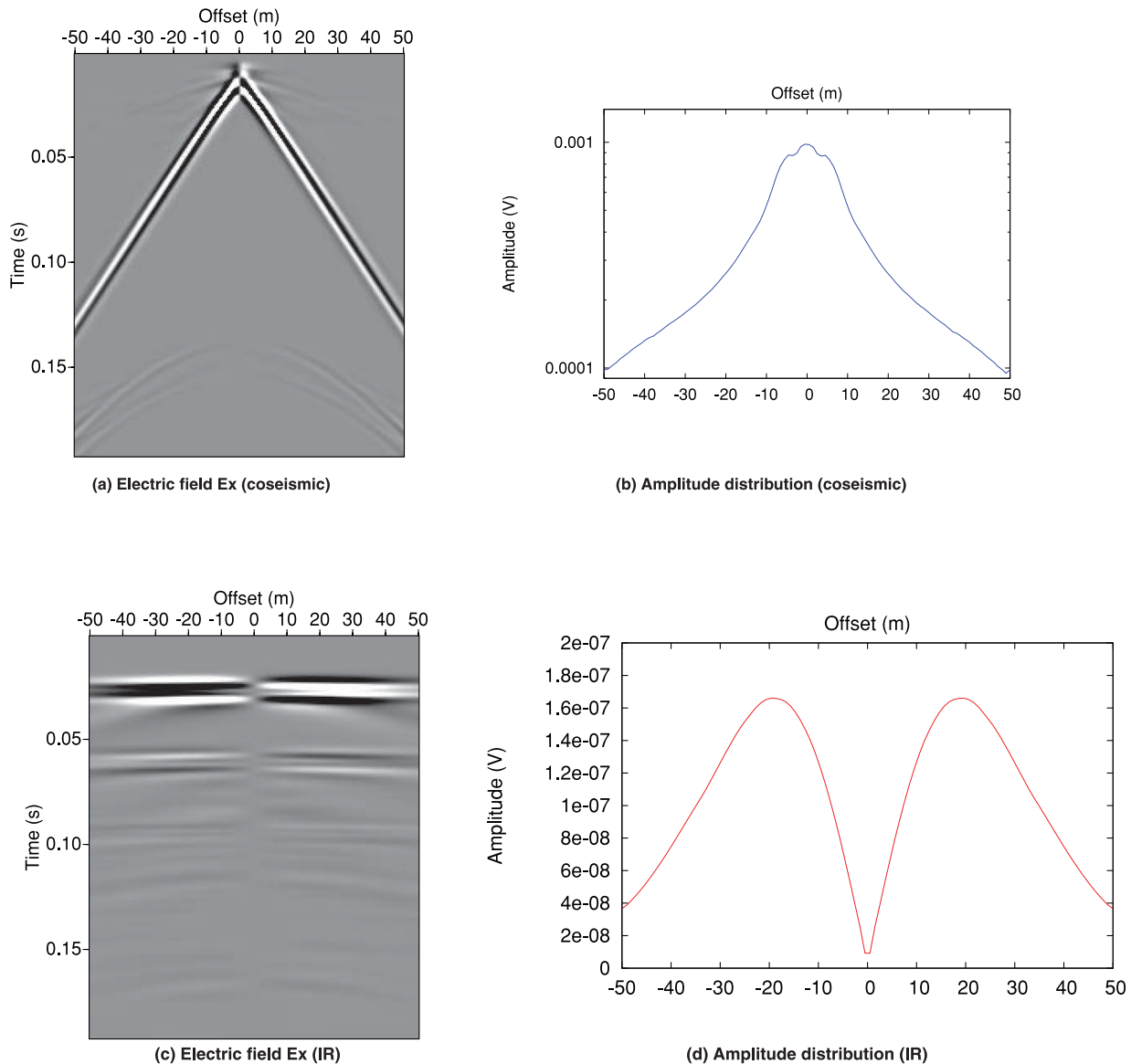
(a) Electric field Ex (coseismic)

(b) Amplitude distribution (coseismic)

(c) Electric field Ex (IR)

(d) Amplitude distribution (IR)

Figure 4. Synthetic electrogram and amplitude distribution for the coseismic wavefield (a) and (b) and for the interface response (c) and (d). The amplitude pattern is the mean distribution computed over a 26-samples wide time window centred on the first interface response, ranging from min = 25 to max = 50.

the maximum coseismic amplitude is only one order of magnitude greater than the maximum IR amplitude).

3 TYPE II/TYPE I WAVE SEPARATION TECHNIQUES APPLIED TO SYNTHETIC DATA

3.1 $f - k$ filtering

Muting in the frequency-wavenumber ($f - k$) domain is a technique commonly applied to conventional seismic data to separate several seismic arrivals based on their slopes or 'dips': it is for example an efficient way of filtering out low-velocity ground roll from seismic data sets. This technique consists in applying a spatial and temporal Fourier transform to the original data, thus sending it in the $f - k$ domain, where events are plotted along lines whose slopes are given by their apparent velocities $v = df/dk$. In this representation, zero-slowness arrivals such as type II converted waves

align along the (vertical) wavenumber axis $k = 0$ and can be recovered using a simple 'pie-slice' filter before Fourier transforming the data back to the conventional time-space ($t - x$) domain, as shown in Fig. 5. Several authors (Haines *et al.* 2007b; Strahser 2007) have used $f - k$ filtering to separate flat IRs from dipping coseismic waves, both on synthetic test gathers and real seismoelectric data.

Although it may successfully highlight the IR, this method suffers from various limitations:

(1) It requires a good spatial resolution, that is an important number of traces. Although this is not an issue when working with synthetic data, it becomes problematic if one has access to a limited number of receivers in the field. Dense spatial sampling can be achieved by combining data from different shotpoints to form supergathers, as proposed by Dupuis *et al.* (2007).
(2) As other velocity-based wave separation techniques, this method does not filter out 'flat' portions of the coseismic signal, such as coseismic reflection hyperbolas near the shotpoint. Haines
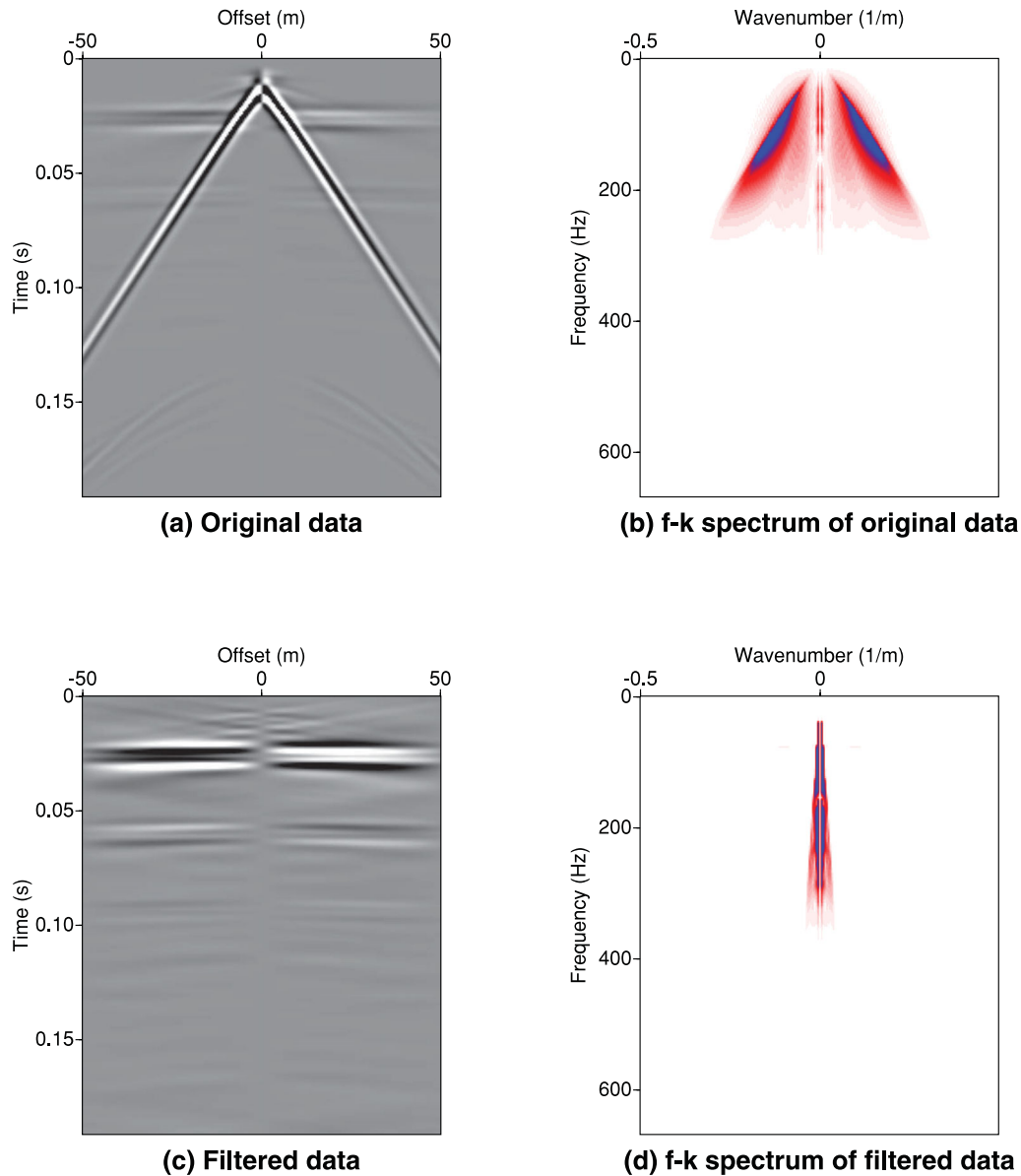
(a) Original data

(b) f-k spectrum of original data

(c) Filtered data

(d) f-k spectrum of filtered data

Figure 5. 'Type II/type I' wave separation through $f - k$ filtering. Synthetic electrograms for which the 'type II/type I' ratio was set to 0.1 are displayed both in time-offset (a) and frequency-wavenumber (b) domains. We have represented the output data (c) as well as its spectrum (d). Samples whose velocities exceeded 4444 m s^{-1} were preserved, whereas those slower than 3703 m s^{-1} were zeroed out.

et al. (2007b) suggest to discard the first few near-offset traces to prevent these horizontal arrivals from masking the type II converted waves.

(3) The type II converted energy may not strictly concentrate along the wavenumber axis, but may leak in other parts of the $f - k$ space, thus overlapping with coseismic energy. The reciprocal is true: parts of the total coseismic energy may smear across the wavenumber axis, thus mixing with the IR. Therefore, separation in $f - k$ domain may significantly alter recovered type II converted signal amplitudes.

$f - k$ filtering appears to alter the recovered IR amplitude pattern. Not only does it degrade the amplitude values, but it also slightly shifts the maxima of the distribution towards greater offsets.

To extract the IR from the synthetic data described in Section 2, we have used the Seismic Unix built-in $f - k$ filter: samples with velocities above 4444 m s^{-1} (0.15$\triangle t/\triangle x$) were retained, although those slower than 3703 m s^{-1} (0.18$\triangle t/\triangle x$) were zeroed out, with tapering applied between these two values to avoid Gibbs effect. These values were chosen because the fastest coseismic direct electric field that needs to be filtered, associated to the P_f wave, travels at 2812 m s^{-1} (0.23$\triangle t/\triangle x$) in our example. The filter's outer slope (0.18$\triangle t/\triangle x$) was chosen after running several tests, in which wider filters ended up with P$_f$ residual energy leaking in the filtered data.

3.2 Radon domain filtering

This method consists in transforming time-offset $(t - x)$ data into the Radon or $\tau - p$ domain, where τ is the intercept time of an event of apparent slowness $p = \frac{1}{V}$, V being the root mean square (rms) velocity. In this representation, events can be filtered out depending on their slowness (Moon *et al.* 1986; Dunne & Beresford 1995).

The Radon transform can be achieved by summing data along various trajectories described by function g:

$$\tau = t - pg(x). \tag{9}$$

We chose to use the linear Radon transform for which $g(x) = x$, as previous work by Haines (2004) suggests it grants better results than the parabolic or hyperbolic transforms when trying to extract the IR. In this case, assuming the original seismic section is described by the function $u(x, t)$, its representation $\tilde{u}(\tau, p)$ in the Radon domain can be defined as:

$$\tilde{u}(\tau, p) = \int_{-\infty}^{\infty} u(\tau + px, x)dx. \tag{10}$$

This straightforward procedure, known as 'slant-stacking', requires data interpolation during both forward and inverse processes, as the slanting line does not necessarily intersect with the traces at the grid points (Claerbout 1986).

This interpolation step may create artefacts: for this reason, one may rather resort to other formulations, such as the 'phase-shift' approach. This approach consists of applying a 1-D Fourier transform to each trace of the original data and multiplying the result by a 'phase shift' factor $e^{-i2\pi f \Delta t}$, where f is the frequency and $\Delta t = px$. According to the Fourier transform translation property, multiplying a function's Fourier transform $U(\omega)$ by a factor $e^{i\omega a}$ (where ω is the angular frequency given in radian) is equivalent to shifting this function u by a constant $+a$ in time domain. Therefore, applying a phase-shift in frequency domain is the same as horizontalizing the summation trajectories in $t - x$ domain. The shifted—or horizontalized—data $U(f, x)e^{-i2\pi f \Delta t}$ can be summed along the x direction, thus leading to $\tilde{U}(f, p)$. This step corresponds to the summation along the slanting line operated in $t - x$ domain, as expressed in eq. (9):

$$\tilde{U}(f, p) = \int_{-\infty}^{\infty} U(f, x)e^{-i2\pi f \Delta t}dx. \tag{11}$$

Applying an inverse 1-D Fourier transform to both sides of eq. (11) finally sends the data in $\tau - p$ domain. When processing synthetic data, we chose to work with the SeismicLab Matlab toolbox, as it provides such a Fourier implementation of the Radon transform.

A linear arrival in the $t - x$ domain (Fig. 6a) collapses to a point in the Radon domain (Fig. 6b). The nearly flat IR translates into a 'cross' located in the vicinity of the zero-slowness axis. This cross is fairly well separated from the higher energy ellipse corresponding to the direct coseismic wavefield. Although this wavefield appears as an elongated stain exhibiting several slowness, its peak amplitude is located at about 2.25×10^{-2} s m^{-1}, that is, the inverse of the 4.40×10^2 m s^{-1} apparent velocity exhibited by the surface waves. Using 201 traces with a slowness pace of $\Delta p = 3 \times 10^{-5}$ s m^{-1} in the Radon domain, wave separation was achieved by keeping the first 7 traces on either sides of the slowness axis (i.e. keeping samples whose velocities exceed 4.76×10^3 m s^{-1}), whereas zeroing out the 85 traces farthest from the slowness axis (i.e. rejecting velocities below 2.22×10^3 m s^{-1}). A cosine ramp was applied to taper the intermediate traces (Fig. 6c).

Filtering in the Radon domain better preserves the relative amplitudes than $f - k$ filtering. The radiation pattern recovered after $\tau - p$ filtering and subsequent amplitude correction (grey line in Fig. 10), matches the theoretical IR amplitude curve (red line in Fig. 10) much more closely than the $f - k$ response does (blue line in Fig. 10). The amplitude correction step was necessary as Radon filtering does not preserve the absolute amplitude values, that is data after forward and inverse slant-stack do not exhibit the same

amplitudes as the original data set, sometimes differing by several orders of magnitude.

To account for this problem, we multiplied the distribution recovered through Radon filtering by an arbitrary factor to fit the theoretical amplitude pattern; this correction by an arbitrary factor is possible within the frame of this study as the theoretical IR is known. However, in real case scenarios, one would need to resort to ρ filters (Claerbout 1986). We have implemented such a filter in time domain and found it granted similar results than the amplitude correction used throughout this paper.

3.3 Filtering in the curvelet domain

'Wavelets' have found a wide range of applications including data compression, denoising and structure extraction (Daubechies 1992; Coifman & Donoho 1995; Moreau *et al.* 1997; Mallat 1999; Saracco *et al.* 2007; Mauri *et al.* 2010; Ma & Plonka 2010; Mauri *et al.* 2012) and are now extensively used in seismic data processing (Roueff *et al.* 2006). A seismic trace can indeed be expressed in terms of 1-D discrete wavelets $\Psi_{(j,k)}$, which are dilated and translated versions of a 'mother' wavelet Ψ, an oscillating function of compact support. As seismic traces can be considered bandwidth limited, the correlation between a seismic reflected event and an analysing wavelet will only be significant if this wavelet displays the same frequency content (determined by its scale j: the higher the scale, the lower the frequency content) and is localized at the same time as the event (controlled by its translation parameter k). Therefore, correlating a seismic trace with appropriate wavelets leads to a 'sparse' representation of the signal, that is, a representation for which most of its energy is represented over a small number of coefficients.

1-D wavelets thus enable to detect singularities and analyse individual traces, but do not take advantage of the geometrical features displayed by trace collections. Characterizing 2-D features of seismic and seismoelectric wave fronts needs specific wavelet representations which do not only involve dilating and translating, but also rotating the mother wavelet. The rotation operator has been introduced early in the theory of continuous wavelets (Murenzi 1990; Antoine *et al.* 1993) and related to the Radon transform (Holschneider 1991), thus leading to the so-called ridgelet transform. This transform combines a 1-D wavelet transform with a Radon transform providing sparse representation of straight line features within a 2-D image (Candès 1998; Candès & Donoho 1999a). To better represent curved features, the curvelet transform was first introduced as a series of local ridgelet transforms (Candès & Donoho 1999b); it was then optimized in terms of coronal representation (Candès *et al.* 2006; Fadili & Starck 2009). Therefore, as compared to the 1-D wavelet transform, the curvelet transform is controlled by the orientation index l in addition to the scale index j and translation indices $k = (k_1, k_2)$.

In the field of seismic processing, 2-D curvelets have been applied to ground roll removal (Zhang *et al.* 2010; Zheng *et al.* 2011) and to aliased data interpolation (Chauris & Nguyen 2008). They have also been used for primary-multiple separation through either non-linear optimization through a block-coordinate relaxation algorithm (Herrmann *et al.* 2008) or by using a Bayesian formulation (Saab *et al.* 2007; Wang *et al.* 2007). This Bayesian approach was also adapted to ground roll suppression by Yarham & Herrmann (2008).

We use here the 'wrapping' implementation of the Fast Discrete Curvelet Transform introduced by Candès *et al.* (2006) and implemented both in Matlab and C++ through the CurveLab

toolbox (available at www.curvelet.org). For this implementation, both the forward and inverse transforms are computed over a short time proportional to $n^2\log(n)$ for a $n \times n$ Cartesian input matrix.

The curvelet transform provides a partition of the $f - k$ domain using small windows, or tiles, each of them corresponding to a specific scale, or frequency band, and a specific direction, or angle (Fig. 7). Following the second dyadic decomposition, the number of tiles doubles with every other scale: the finer the scale, the greater the number of tiles paving it (Candès & Demanet 2005; Candès *et al.* 2006). A common approach proposed to suppress—or at least reduce—ground roll from classical seismic data consists in zeroing entire tiles containing the coherent noise. By allowing to select the frequency bands at which surface waves can be observed although leaving the other scales untouched, this strategy takes advantage of the generally lower frequency content of the ground roll with

respect to volume waves (Boeniger *et al.* 2006). However, it cannot be directly applied to our wave separation problem, as type I and type II waves may display close frequency contents. This similarity between frequency contents implies that tiles at all scales must be filtered, a process which effectively comes down to applying a $f - k$ filter. For this reason we introduce here a new filtering strategy taking advantage of the similarities between seismic data and the type I signal.

We expressed both the seismic acceleration and the seismoelectric data in the curvelet domain, using a 5-scale decomposition with 32 angles at the second coarsest scale; complex-valued coefficients were considered, and wavelets were used at the finest scale. A representation of the curvelet coefficients for the seismoelectric data is displayed in Fig. 8(a) for the first three scales: the coarse scale is represented at the centre, although the two concentric coronae surrounding it correspond to levels 2 and 3.
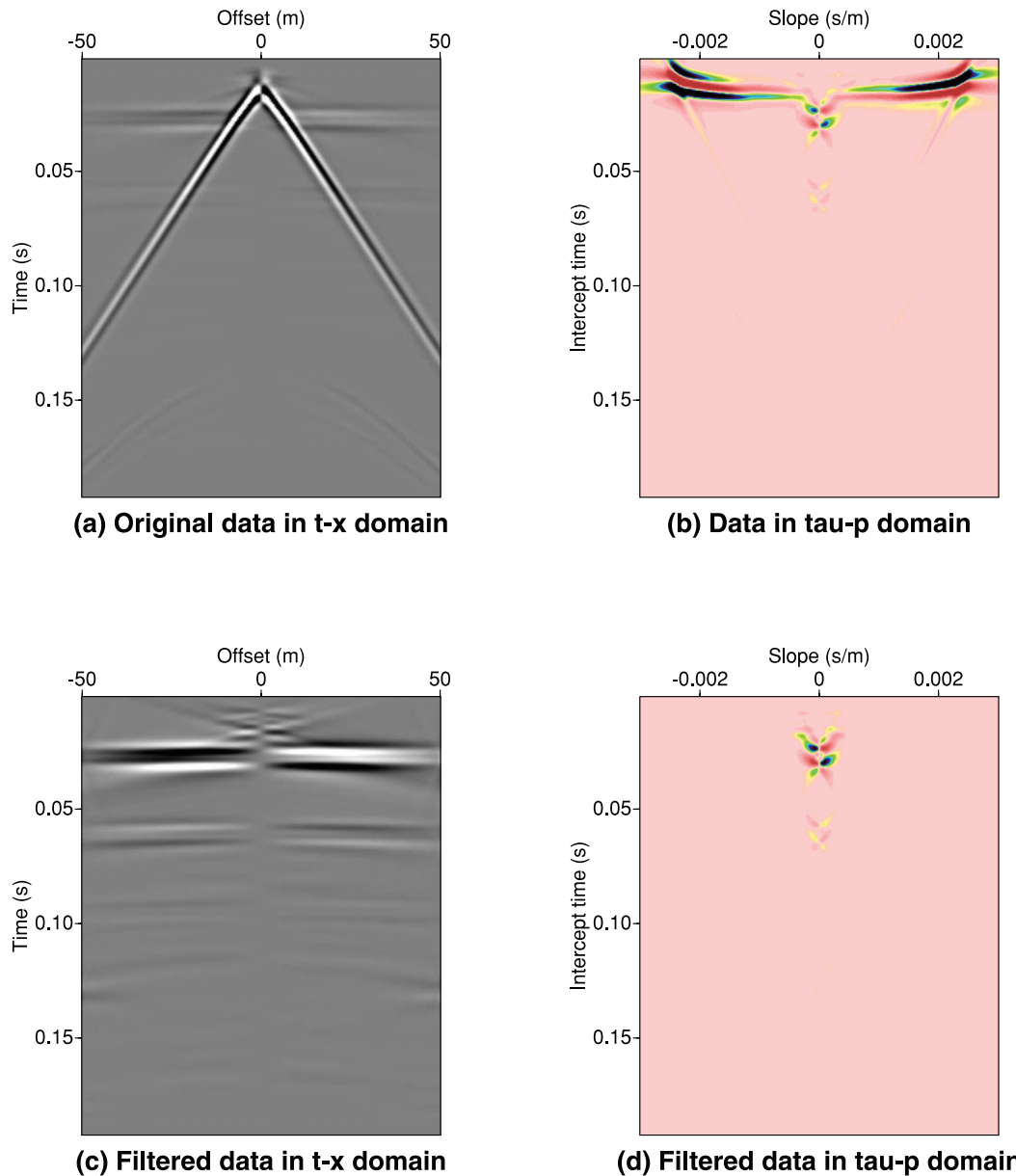

(a) Original data in t-x domain

(b) Data in tau-p domain

(c) Filtered data in t-x domain

(d) Filtered data in tau-p domain

Figure 6. 'Type II/type I' wave separation through Radon-domain filtering. Synthetic electrograms for which the 'type II/type I' ratio was set to 0.1 are displayed both in time-offset (a) and intercept time-slowness (b) domains. We have represented the output data (c) as well as its $\tau - p$ representation (d). Velocities above 4761 m s^{-1} were preserved, whereas those below 2222 m s^{-1} were rejected.

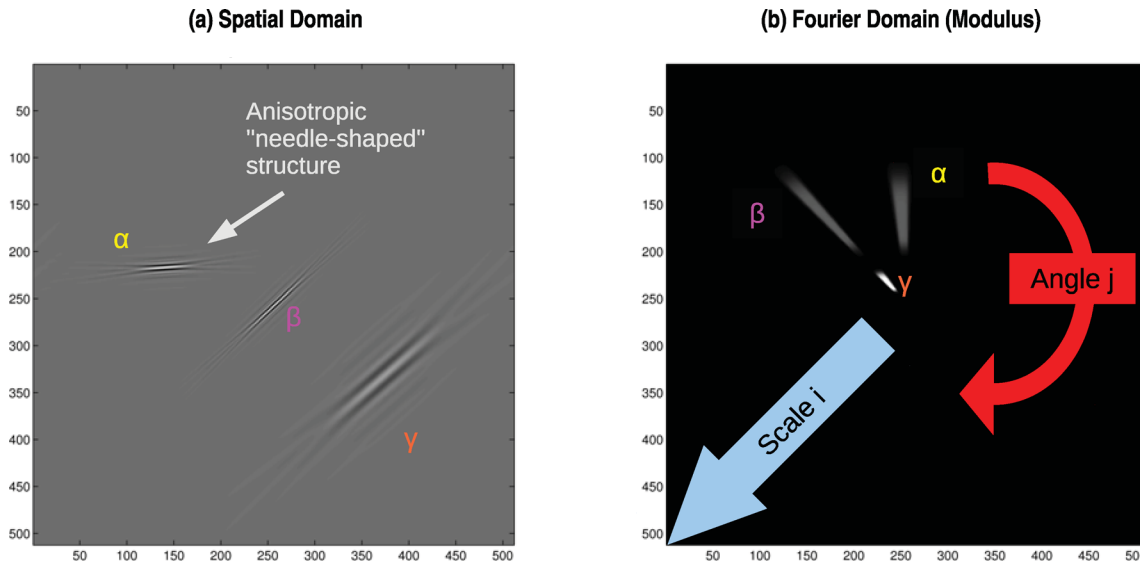**(a) Spatial Domain**   **(b) Fourier Domain (Modulus)**

Figure 7. Some curvelets generated with CurveLab for different scales, orientations and positions, displayed both in spatial and frequency (Fourier) domain. Six scales are used here, represented as concentric coronae on the Fourier domain pseudo-polar tiling. α and β share the same scale but have different orientations and positions; β and γ share the same orientation but have different scales and positions. The number of orientations doubles every other scale, so the frequency support for γ appears as a wedge twice as wide as the α and β wedges. This figure shows that horizontal events in the time-offset domain such as α are transformed onto vertical wedges in the Fourier domain: our mask will take advantage of these features by favouring these central tiles.

The coarse scale is a matrix oriented like the original image. Indeed, it looks like a blurry version of the original data for which only the low frequency features appear. The individual tiles forming the outer coronas do not follow this orientation: they are instead aligned with the rotating analysing curvelet. A look at the second corona (i.e. intermediate scale 3) reveals that the correlation between the analysing curvelet at this scale and the data is highest for tiles 19 and 30, counting clockwise from the top left corner. Identifying the tiles with maximum correlation coefficient values for all other scales allows to note that the maximum energy is concentrated along directions roughly $\pm 60°$ away from the horizontal direction, corresponding to the coseismic surface waves visible in Fig. 3(c). Therefore, exactly like in $t - x$ domain, the seismoelectrics recording represented in curvelet domain are dominated by coseismic Rayleigh waves. These strong arrivals conceal the IR which would otherwise appear in the central tiles 8 and 9 aligned with the horizontal direction.

As the coseismic horizontal electric wavefield should be directly related to the horizontal seismic acceleration, we expressed the latter in the curvelet domain to build a mask to apply to seismoelectric data. A scale-dependent, angle-dependent threshold function $T(j, l)$ was chosen as:

$$T(j, l) = E(j)\Gamma(l), \tag{12}$$

where $E(j)$ is the total energy at each intermediate scale j and $\Gamma(l)$ is an angle-dependent Gaussian function centred around the horizontal directions:

$$\Gamma(l) = \begin{cases} e^{-\left(l - \frac{1}{2} - \frac{1}{8}N_j\right)^2}, & l \in \left[1; \frac{3}{8}N_j\right] \\ e^{-\left(l - \frac{1}{2} - \frac{5}{8}N_j\right)^2}, & l \in \left[\frac{3}{8}N_j + 1; \frac{1}{2}N_j\right]. \end{cases} \tag{13}$$

In eq. (13), N_j is the total number of angles at the considered scale. This Gaussian term ensures thresholding becomes less selective near the horizontal direction, where most of the IR energy is found, and penalizes the greater angles, dominated by the lower velocity coseismic field.

Acceleration coefficients in the curvelet domain were compared to $T(j, l)$: where their amplitude exceeded the threshold, the mask values were zeroed, otherwise they were set to 1. The coarse layer was arbitrarily set to 0 (equivalent to a high-pass filter), although a $f - k$ filter was applied to the finest scale, as data at this detailed scale have the same dimension as the original time-offset data. The resulting mask is displayed in Fig. 8(b), with zero values in black and values set to 1 in white: one can see it preserves the vertical tiles, that is the horizontal directions. The threshold used here enabled to filter out specific samples 'within' each tile, instead of aggressively cancelling entire windows. Data obtained after filtering are depicted in Fig. 8(c) in the curvelet domain: events that were invisible in Fig. 8(a) can now be clearly seen in white in the 'vertical' tiles. These events correspond to the horizontal arrivals observed when transforming back the filtered data to the time-offset domain (Fig. 9). Although three flat events can be noted on this seismoelectrogram, it can be deduced from their arrival times that only the earliest response is an actual IR: the two later arrivals correspond to multiple reflections.

4 COMPARISON BETWEEN THE DIFFERENT TECHNIQUES

Among the three methods presented here, filtering in the curvelet domain seems to grant the best results in terms of recovered amplitudes, as shown by the black dotted line in Fig. 10. An objection can be raised regarding the far-offsets at which the consistency between recovered and theoretical models deteriorates. This behaviour could be explained by the fact that the IR is truncated on the left and right sides of the image before it can gently fall down to zero. Curvelets provide optimally sparse representations of objects which display 'curve-punctuated smoothness' (Candès *et al.* 2006), but in this case, the smoothness is disturbed as the wave front is truncated.
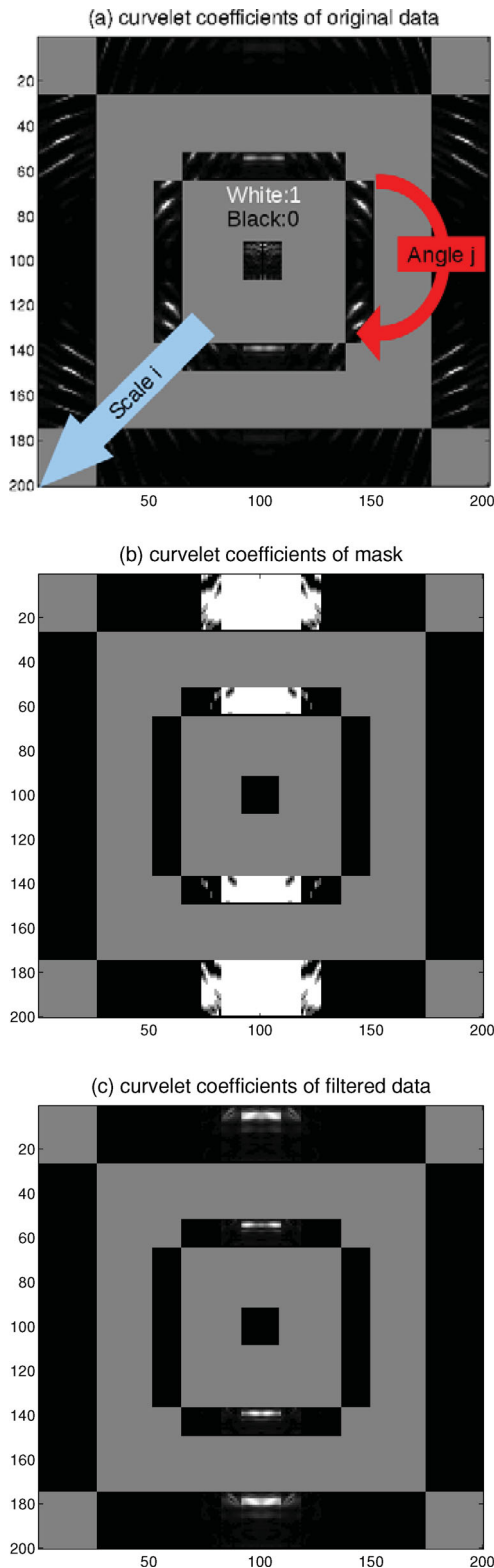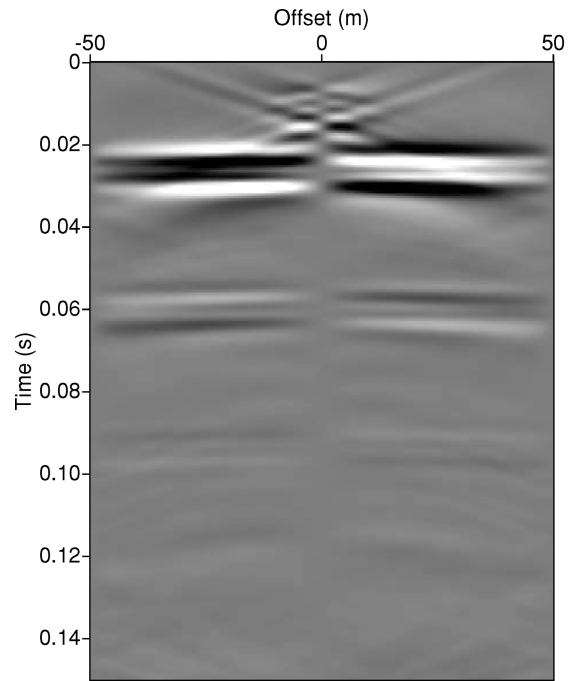
(a) curvelet coefficients of original data

White:1
Black:0

Angle j

Scale i

(b) curvelet coefficients of mask

(c) curvelet coefficients of filtered data

Figure 8. Curvelets coefficients for the first three scales for (a) the original seismoelectric data, (b) the mask deduced from seismic acceleration and (c) the seismoelectric data after applying this mask. Zero values are depicted in black, whereas values set to one are represented in white.

Data after filtering in the curvelet domain

Figure 9. Interface response recovered after filtering in the curvelet domain.

To investigate the sensitivity of the aforementioned methods to non-coherent noise, different levels of WGN were added to the electric data, corresponding to signal-to-noise (S/N) ratios of 5, 10, 20 and 50. The results are displayed in Fig. 11. Radon domain filtering seems less affected by non-coherent noise than the other filtering techniques, for which it becomes hard to recover the IR under a S/N ratio of 5. This result can be explained by the very nature of the Radon transform, for which data are summed along slanting lines: adding together a series of small perturbations of opposite signs overall helps reduce the non-coherent noise.

Until now, we have worked with a 'type II/type I' ratio of 0.1, a fairly favourable case for which the maximum amplitude of the IR amplitude is only 10 times weaker than the amplitude of the coseismic surface waves electric field amplitudes. However, according to the modelling tests we ran, this ratio may be much smaller. To account for a more realistic situation, we have tested our filtering techniques on data with a 'type II/type I' ratio of 0.01.

Although the IRs modelled in both tests have the same dip (i.e. both of them are horizontal), applying the different filters with the same parameters as the ones previously used grants poor results, with the recovered amplitude patterns being deformed. To remove the much stronger surrounding coseismic signal, one needs to adjust the parameters to create narrower filters than the ones used before. The results on the amplitude distribution are displayed in Fig. 12. The new parameters used to filter out these data are:

(1) **Frequency-wavenumber $f - k$ filtering:** data points with velocities above 5128 m s^{-1} were kept, although those with velocities smaller than 4166 m s^{-1} were zeroed out.

(2) **Radon filtering:** data points with velocities above 5555 m s^{-1} were kept, although those with velocities smaller than 3030 m s^{-1} were zeroed out.
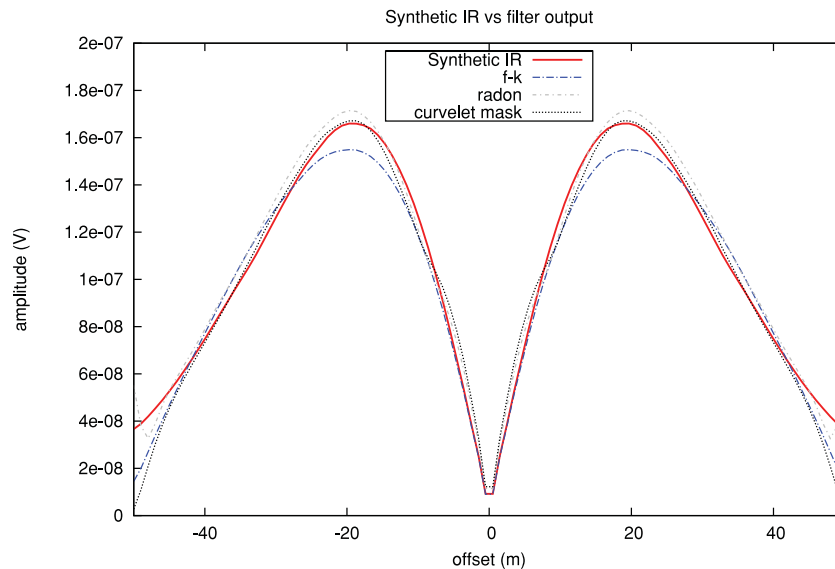
Synthetic IR vs filter output

Figure 10. Amplitude distribution for the interface response recovered through various wave separation techniques: $f - k$ filtering, Radon domain filtering and filtering in the curvelet domain. The amplitude pattern for the synthetic interface response from Fig. 4(d) was also displayed for comparison. Note that although Radon domain filtering preserves the relative amplitudes, the distribution recovered through this method had to be multiplied by an arbitrary factor to match the theoretical response.

(3) **Curvelet domain filtering:** we modified the threshold function $\Gamma(l)$ to make it slightly narrower by multiplying the term under the exponential by 2.5.

Both the $f - k$ and the Radon outputs display an unexpected decrease in amplitude near the offset for which they should be maximal. This decrease indeed corresponds to the portion of coseismic signal that could not be removed through filtering, thus interfering with the IR. The results obtained through curvelet filtering seem to better fit the theoretical IR.

5 FILTERING FIELD OBSERVATIONS

The data used to test the filtering techniques are those presented by Garambois & Dietrich (2001). They were acquired along the Fier river, near Annecy (France). The subsurface in this area consists of alluvial deposits interwoven with gravel, sand and clay layers down to a depth of 150 m, with a water table located at a depth of 1.5 m. Fig. 13 displays the electric field obtained by using an explosive source consisting of a 200 g dynamite charge buried 1 m below the surface. Twenty-four 1-m-long dipoles were deployed on either sides of the shotpoint, with a receiver pair located 5 m from the shotpoint, and dipoles evenly spaced between 10 and 30 m, with a 1 m receiver spacing.

Several harmonics of the power line frequency (50 Hz) taint the signal: we applied the 'block subtraction' method (Butler 1993) to reduce this noise. This method involves recording data during a time interval for which the non-harmonic components of the signal are assumed negligible, typically before triggering the source. The obtained noise block is then shifted and subtracted from the original record. As no electric data were recorded before triggering the source, the record's last 200 samples (i.e. the last 0.02 s) were supposed free of any signal; an estimate of the harmonic noise was built from this block, which was then removed from the original data.

Coseismic Rayleigh waves clearly dominate the record, but high-frequency events can also be seen. Garambois & Dietrich (2001)

highlighted these by applying a simple zero-phase bandpass filter between 160 and 600 Hz. Three elements were invoked to relate these events to the IR: (1) their opposite polarities on either sides of the shotpoint, (2) their amplitude distribution, which does not decrease as rapidly as it would be the case for coseismic arrivals and (3) their high apparent velocity.

$f - k$, Radon and curvelet filters were applied to these data, after a preliminary high-pass filter was used to remove events of frequency below $f_c = 40$ Hz. Results are displayed in Fig. 14, for two selected time windows containing three IRs labelled A, C and D, which were discussed in Garambois & Dietrich (2001). For the sake of comparison, Fig. 14 also displays the original seismoelectric data before filtering (a and b), as well as the bandpass filtered data (a* and b*), using the 160–600 Hz filter formerly used in Garambois & Dietrich (2001). Near-offset traces at ± 5 m were used only with the bandpass and $f - k$ filter. The programs used for Radon and curvelet filtering required regular spatial sampling, so we processed only the traces located between ± 10 and 30 m.

All four filtering techniques allow to successfully enhance the IRs. The bandpass filtering output is relatively noisy compared to the output obtained with other methods, especially for later arrival times, as can be seen in Fig. 14(b*). However, the bandpass filter works quite well at highlighting the investigated events. This good performance raised the question of why bothering to deploy more complex methods. It should be stressed that this decent performance is rather an exception than the common rule, as IRs have often been reported to exhibit the same frequency content as the seismic waves that created them (Pride & Garambois 2002; Haines *et al.* 2007b). Furthermore, looking at the central traces after 10 ms (Fig. 14a*) shows that part of the total coseismic energy was not rejected through bandpass filtering: this residual coseismic signal indeed calls for the use of other filters. Results obtained through Radon filtering seem artificially biased towards lower frequencies: although the recovered seismoelectrograms look cleaner than those obtained through bandpass or $f - k$ filtering, the events lose much of their sharpness at greater offsets, therefore being harder to precisely locate in time. Of all four methods, curvelet filtering seems to grant
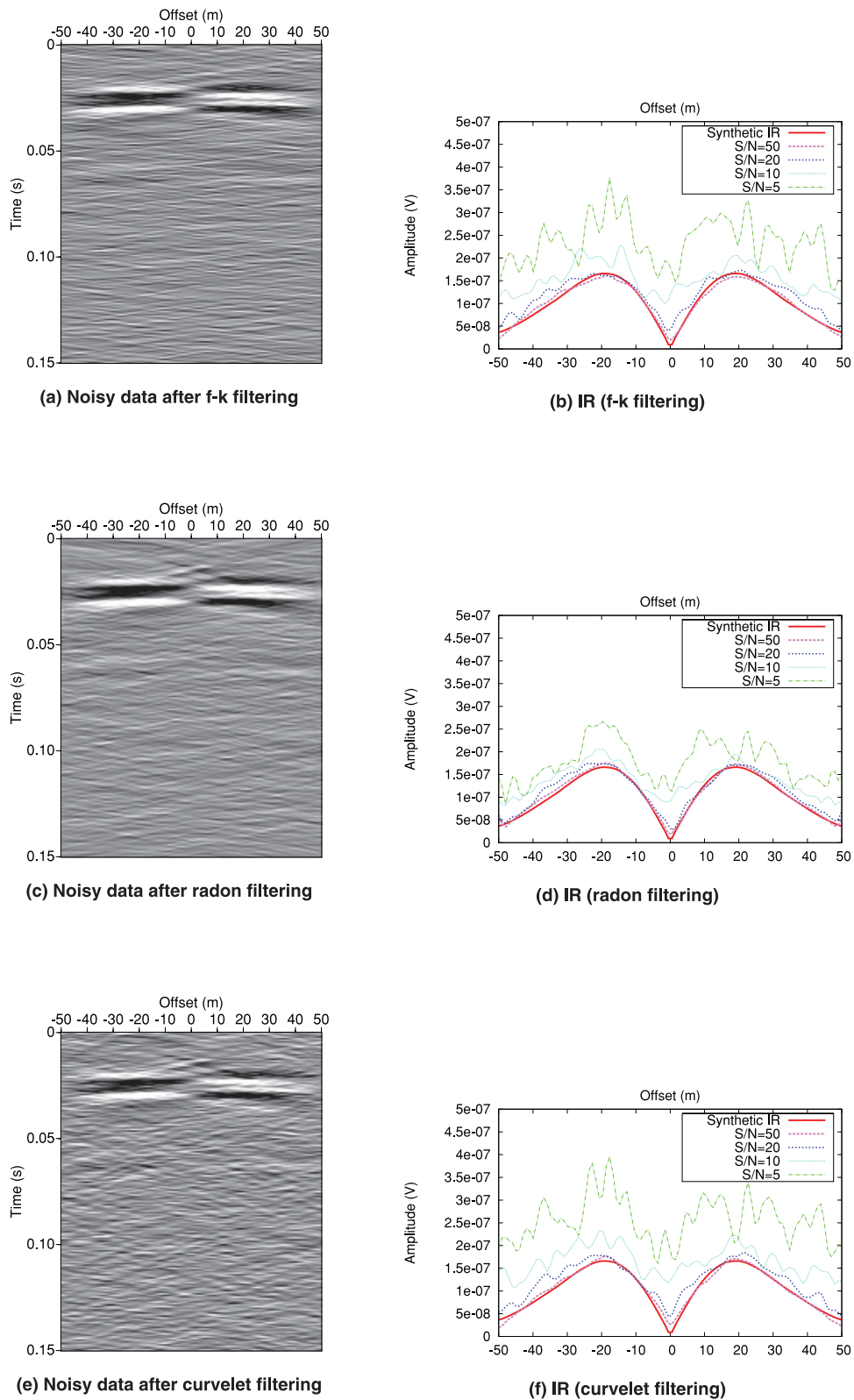
(a) Noisy data after f-k filtering

(b) IR (f-k filtering)

(c) Noisy data after radon filtering

(d) IR (radon filtering)

(e) Noisy data after curvelet filtering

(f) IR (curvelet filtering)

Figure 11. Sensitivity of the wave-separation techniques to White Gaussian Noise. Examples of noisy recordings are displayed on the left-hand side figures ((a) $(f - k)$, (c) $(\tau - p)$ and (e) filtering in the curvelet domain). The associated amplitude patterns for different S/N are plotted on (b), (d) and (f).
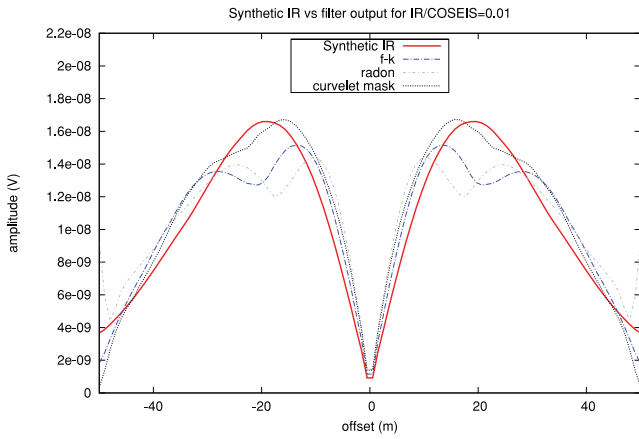
Figure 12. Amplitude distribution for the interface response recovered through various wave separation techniques: $f - k$ filtering, Radon domain filtering and filtering in the curvelet domain, this time using a 'type I/type II' ratio of 0.01 (i.e. for which the interface response is at least 100 times smaller than the maximum coseismic amplitude). The amplitude pattern for the synthetic interface response from Fig. 4(d) was also displayed for comparison.

the best results. It works better at early times than the other filters, highlighting an event at 5 ms that was barely visible on the original data and on the $f - k$ output. One may argue that the electrograms obtained after Radon and curvelet filtering look fairly similar: it is therefore necessary to take a look at the way these filtering techniques affect the signal amplitudes to distinguish the benefits of the curvelet approach.

The amplitude distributions recovered after filtering for event A are displayed in Fig. 15. For this specific event, it can be said that the radiation pattern recovered through curvelet filtering output resembles the most to the bandpass filtering output. This similarity is not surprising as we zeroed both the higher and lower scales (i.e. the central tile and outer corona) during the curvelet filtering process. This similarity between both methods was less obvious for events C and D, for which the results are not displayed here. However, a feature common to all three events is that both $f - k$ and Radon methods seem to slightly underestimate the signal

amplitude compared to the curvelet technique, as was predicted by our modelling tests (Fig. 12).

6 CONCLUSION AND PERSPECTIVES

When working with seismoelectric surface acquisition geometries, only the IR (or type II signal) can illuminate conversions at depth, as opposed to the coseismic wavefield (or type I signal), which provides information limited to the vicinity of the receivers. Therefore, extracting type II signals from the seismoelectrograms is a crucial step in the seismoelectric data processing workflow. Unfortunately, it is also a difficult one, as these arrivals usually display weak amplitudes. Merely highlighting the IRs can be achieved through common 'dip-based' procedures taking advantage of the EM velocity at which they travel, which is several orders of magnitude greater than those of the coseismic waves.

However, these methods may alter signal amplitudes which are useful when trying to characterize reservoir geometries (Thompson *et al.* 2007).

In this paper, we studied the effect of various filtering methods on type II signal amplitudes and waveforms. We introduced a new filtering procedure, based on specific 2-D multiscale and multidirectional wavelets called 'curvelets'. This method combines our prior knowledge of the coseismic wavefield deduced from the seismic accelerations with our prior knowledge of the zero-slowness exhibited by IRs, by using a Gaussian threshold function centred around the horizontal dips.

This filtering strategy in curvelet domain was compared to two dip-based methods, the $f - k$ and Radon domain filters. When applied to synthetic data with a type II/type I ratio of 0.1, this new method provided the best results in terms of amplitude preservation: the radiation pattern recovered through this procedure closely resembled the theoretical amplitude distribution that we modelled independently from the coseismic wavefield. However, the similarity between both plots was not convincing for large offsets, for which the IR was artificially truncated. As the smoothness of the seismoelectric wave front was locally disturbed, it could no longer be properly described by curvelets. These results were confirmed for a less favourable but more realistic type
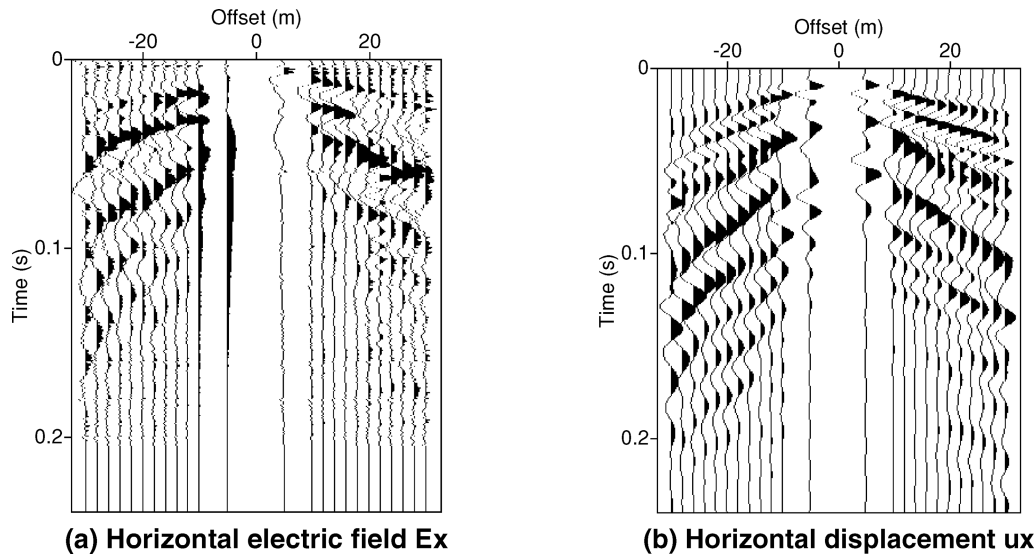

(a) Horizontal electric field Ex

(b) Horizontal displacement ux

Figure 13. Electric and seismic data acquired near the Fier river in Annecy, France (Garambois & Dietrich 2001). Block subtraction was performed on the electric data to remove the power line harmonics.
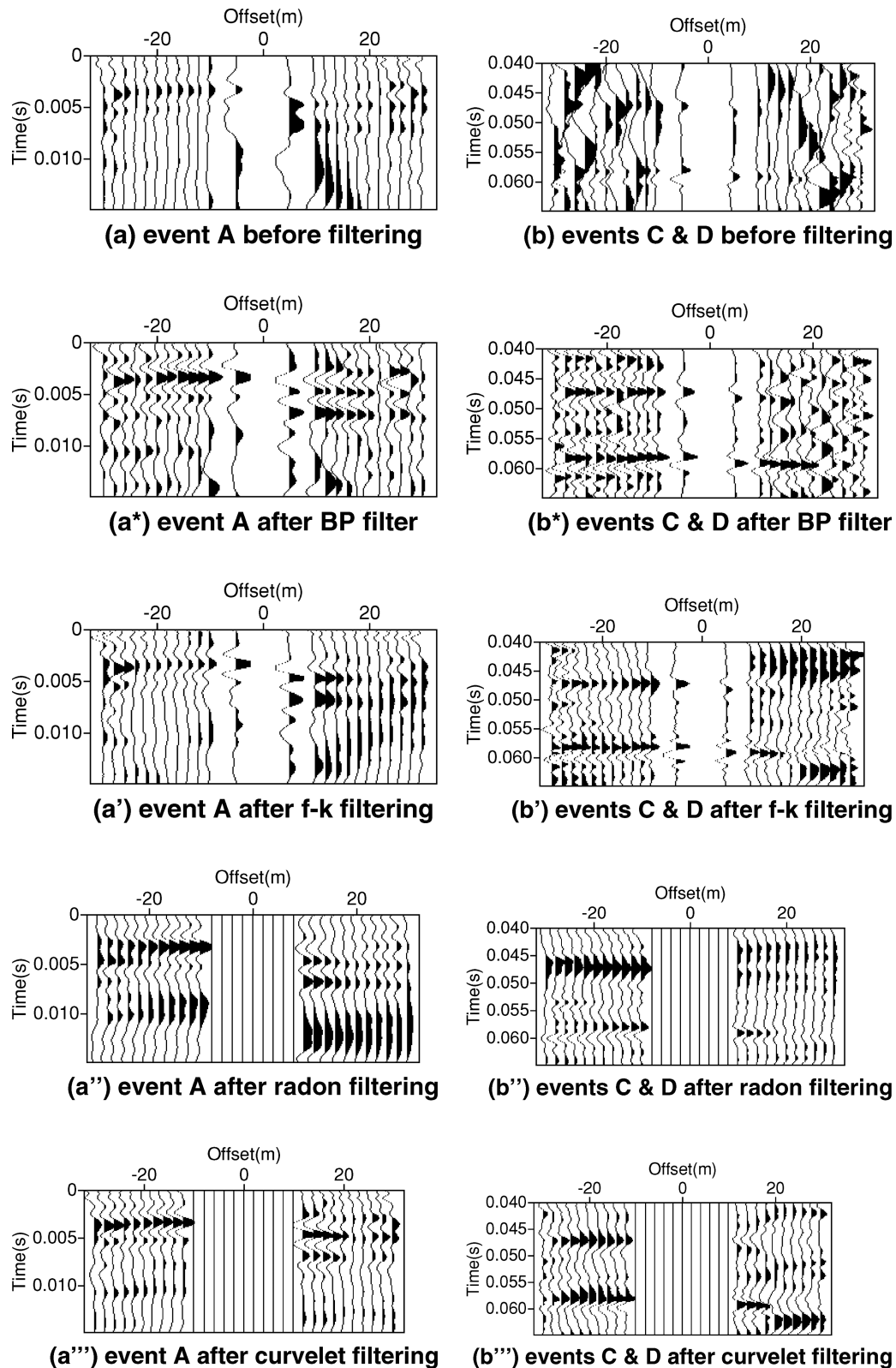
Figure 14. Measured electric field signals, before (a and b) and after bandpass filtering (a* and b*), $f - k$ filtering (a' and b'), Radon domain filtering (a'' and b'') and curvelet filtering (a''' and b'''). Events A, C and D were discussed in Garambois & Dietrich (2001).
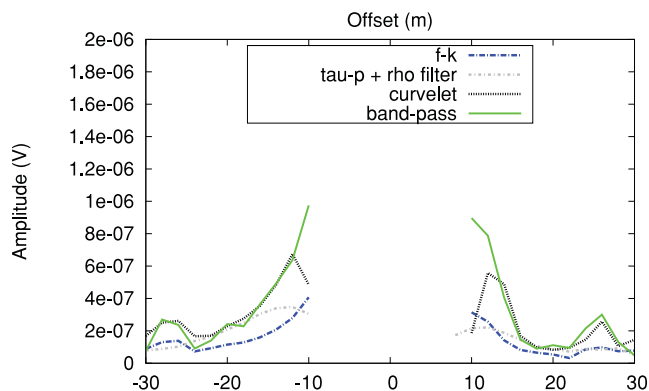
Figure 15. Amplitude distribution for event A after applying different filtering techniques. Results for offsets between 10 m were not displayed as these central traces were not used for curvelet and Radon filtering.

II/type I ratio of 0.01. We also tested the sensitivity of all three methods to various levels of WGN: it turned out that Radon filtering was less affected by this non-coherent noise than other techniques.

We also tested these techniques with a set of real data acquired by Garambois & Dietrich (2001) in sedimentary deposits. We compared our results with those obtained with a simple bandpass filter applied by the authors. Curvelet filtering enabled to successfully recover all three previously investigated IRs, although returning a radiation pattern very similar to the one obtained through bandpass filtering in the case of the earliest event. As it was predicted by our simulations, $f - k$ filtering seemed to underestimate the signal amplitudes compared to curvelet filtering and amplitude-corrected Radon filtering, the correction being performed either by multiplicating the filter output by an arbitrary factor or by applying a ρ filter. It can also be added that the Radon transform appeared to bias the data towards the low frequencies. Overall, curvelet filtering seemed to work better than the other methods, revealing flat events that were barely visible through the use of other filtering techniques.

At the moment, our understanding of the relation between the full coseismic wavefield and the seismic diplacements/velocities/accelerations remains unclear. For the case of a simple homogeneous and isotropic space and by working in the low-frequency range, Garambois & Dietrich (2001) have derived the transfer function relating the volume waves acceleration and their associated coseismic electric field. Such a transfer function has not yet been established for surface waves but would constitute a crucial step in the coseismic wavefield removal process. One could bring our work one step further by devising a wave-separation method combining (1) classical 'dip-based' filters to remove only low-velocity surface waves with (2) further filtering taking advantage of our knowledge of the transfer function between volume waves and their coseismic counterparts to elaborate a more refined mask in the curvelet domain.

ACKNOWLEDGMENTS

REFERENCES

Allègre, V., Jouniaux, L., Lehmann, F. & Sailhac, P., 2010. Streaming potential dependence on water-content in Fontainebleau sand, *Geophys. J. Int.,* **182,** 1248–1266.

Allègre, V., Lehmann, F., Ackerer, P., Jouniaux, L. & Sailhac, P., 2012. A 1D modelling of streaming potential dependence on water content during drainage experiment in sand, *Geophys. J. Int.,* **189**(1), 285–295.

Antoine, J., Carrette, P., Murenzi, R. & Piette, B., 1993. Image analysis with two-dimensional continuous wavelet transform, *Signal Process.,* **31,** 241–272.

Block, G.I. & Harris, J.G., 2006. Conductivity dependence of seismoelectric wave phenomena in fluid-saturated sediments, *J. geophys. Res.,* **111,** B01304, doi:10.1029/2005JB003798.

Boeniger, U., Herrmann, F.J. & Yarham C., 2006. Curvelet-based ground roll removal, *Seg Tech. Program Expanded Abstr.,* **25**(1), 2777–2782.

Bordes, C., Jouniaux, L., Dietrich, M., Pozzi, J.-P. & Garambois, S., 2006. First laboratory measurements of seismo-magnetic conversions in fluid-filled Fontainebleau sand, *Geophys. Res. Lett.,* **33,** L01302, doi:10.1029/2005GL024582.

Bordes, C., Jouniaux, L., Garambois, S., Dietrich, M., Pozzi, J.-P. & Gaffet, S., 2008. Evidence of the theoretically predicted seismo-magnetic conversion, *Geophys. J. Int.,* **174,** 489–504.

Bouchon, M., 1981. A simple method to calculate Green's functions for elastic layered media, *Bull. seism. Soc. Am.,* **71**(4), 959–971.

Bouchon, M. & Aki, K., 1977. Discrete wave-number representation of seismic-source wave fields, *Bull. seism. Soc. Am.,* **67**(2), 259–277.

Butler, K.E., 1993. Subtraction of powerline harmonics from geophysical records, *Geophysics,* **58**(6), 898–903, doi:10.1190/1.1443474.

Candès, E., 1998. Ridgelets: theory and applications, *PhD thesis,* Department of Statistics, Stanford University.

Candès, E. & Donoho, D., 1999a. Ridgelets: the key to high dimensional intermittency?, *Phil. Trans. R. Soc. Lond., A.,* **357,** 2495–2509.

Candès, E. & Donoho, D., 1999b. Curvelets—a surprisingly effective non-adaptive representation for objects with edges, in *Curve and Surface Fitting,* eds Cohen, A., Rabut, C. & Schumaker, L.L., Vanderbilt University Press, Nashville, TN.

Candès, E.J. & Demanet, L., 2005. The curvelet representation of wave propagators is optimally sparse, *Commun Pure Appl. Math.,* **58**(11), 1472–1528.

Candès, E., Demanet, L., Donoho, D. & Ying, L., 2006. Fast discrete curvelet transforms, *Multiscale Model. Simul.,* **5**(3), 861–899, doi:10.1137/05064182X.

Chauris, H. & Nguyen, T., 2008. Seismic demigration/migration in the curvelet domain, *Geophysics,* **73**(2), S35–S46.

Chen, B. & Mu, Y., 2005. Experimental studies of seismoelectric effects in fluid-saturated porous media, *J. geophys. Eng.,* **2,** 222–230.

Claerbout, J.F., 1986. Imaging the earth's interior, *Geophys. J. Int.,* **86**(1), 217–217.

Coifman, R.R. & Donoho, D.L., 1995. Translation-invariant denoising, Tech. Rep., CiteSeerX.

Daubechies, I., 1992. *Ten Lectures on Wavelets,* Society for Industrial and Applied Mathematics, Philadelphia, PA.

Davis, J.A., James, R.O. & Leckie, J., 1978. Surface ionization and complexation at the oxide/water interface, *J. Colloid Interface Sci.,* **63,** 480–499.

Dunne, J. & Beresford, G., 1995. A review of the t-p transform, its implementation and its applications in seismic processing, *Explor. Geophys.,* **26**(1), 19–36.

Dupuis, J.C. & Butler, K.E., 2006. Vertical seismoelectric profiling in a borehole penetrating glaciofluvial sediments, *Geophys. Res. Lett.,* **33,** 5, doi:10.1029/2006GL026385.

Dupuis, J.C., Butler, K.E. & Kepic, A.W., 2007. Seismoelectric imaging of the vadose zone of a sand aquifer, *Geophysics,* **72**(6), A81–A85, doi:10.1190/1.2773780.

Dupuis, J.C., Butler, K.E., Kepic, A.W. & Harris, B.D., 2009. Anatomy of a seismoelectric conversion: measurements and conceptual modeling in boreholes penetrating a sandy aquifer, *J. geophys. Res.,* **114,** 9, doi:10.1029/2008JB005939.

Fadili, M. J. & Starck, J.-L., 2009. Curvelets and ridgelets, In *Encyclopedia of Complexity and Systems Science,* Vol. 3, pp. 1718–1738, ed. Robert, M., Springer, New York.

Gao, Y. & Hu, H., 2010. Seismoelectromagnetic waves radiated by a double-couple source in a saturated porous medium, *Geophys. J. Int.,* **181**(2), 873–896.

Garambois, S. & Dietrich, M., 2001. Seismoelectric wave conversions in porous media: field measurements and transfer function analysis, *Geophysics,* **66**(5), 1417–1430.

Garambois, S. & Dietrich, M., 2002. Full waveform numerical simulations of seismoelectromagnetic wave conversions in fluid-saturated stratified porous media, *J. geophys. Res.,* **107,** 18, doi:10.1029/2001JB000316.

Guan, W., Hu, H. & Wang, Z., 2012. Permeability inversion from low frequency seismoelectric logs in fluid saturated porous formations, *Geophys. Prospect.,* in press, doi:10.1111/j.1365-2478.2012.01053.x

Guichet, X., Jouniaux, L. & Catel, N., 2006. Modification of streaming potential by precipitation of calcite in a sand-water system: laboratory measurements in the pH range from 4 to 12, *Geophys. J. Int.,* **166,** 445–460.

Haartsen, M.W. & Pride, S.R., 1997. Electroseismic waves from point sources in layered media, *J. geophys. Res.,* **102**(B11), 24 745–24 769.

Haines S.S., 2004. Seismoelectric imaging of shallow targets, *PhD thesis,* Stanford University.

Haines, S.S. & Pride, S.R., 2006. Seismoelectric numerical modeling on a grid, *Geophysics,* **71**(6), N57–N65.

Haines, S.S., Guitton, A. & Biondi, B., 2007a. Seismoelectric data processing for surface surveys of shallow targets, *Geophysics,* **72**(2), G1–G8.

Haines, S.S., Pride, S.R., Klemperer, S.L. & Biondi, B., 2007b. Seismoelectric imaging of shallow targets, *Geophysics,* **72**(2), G9–G20, doi:10.1190/1.2428267.

Hase, H., Ishido, T., Takakura, S., Hashimoto, T., Sato, K. & Tanaka, Y., 2003. Zeta potential measurement of volcanic rocks from Aso caldera, *Geophys. Res. Lett.,* **23**(30), doi:10.1029/2003GL018694.

Herrmann, F.J., Wang, D. & Verschuur, D.J.E., 2008. Adaptive curvelet-domain primary-multiple separation, *Geophysics,* **73**(3), A17–A21.

Holschneider, M., 1991. Inverse Radon transforms through inverse wavelet transforms, *Inverse Probl.,* **7,** 853–861.

Hu, H. & Gao, Y., 2011. Electromagnetic field generated by a finite fault due to electrokinetic effect, *J. geophys. Res.,* **116,** 14, doi:10.1029/2010JB007958.

Hu, H., Guan, W. & Harris, J.M., 2007. Theoretical simulation of electroacoustic borehole logging in a fluid saturated porous formation, *J. acoust. Soc. Am.,* **122**(1), 135–145.

Hunt, C.W. & Worthington, M.H., 2000. Borehole elektrokinetic responses in fracture dominated hydraulically conductive zones, *Geophys. Res. Lett.,* **27**(9), 1315–1318.

Jaafar, M.Z., Vinogradov, J. & Jackson, M.D., 2009. Measurement of streaming potential coupling coefficient in sandstones saturated with high salinity NACL brine, *Geophys. Res. Lett.,* **36,** L21306, doi:10.1029/2009GL040549.

Johnson, D.L., Koplik, J. & Dashen, R., 1987. Theory of dynamic permeability and tortuosity in fluid saturated porous media, *J. Fluid. Mech.,* **176,** 379–402, doi:10.1017/S0022112087000727.

Jouniaux, L. & Ishido, T., 2012. Electrokinetics in earth sciences: A tutorial, *Int. J. Geophys.,* **2012,** 1–16.

Jouniaux, L., Pozzi, J.-P., Berthier, J. & Massé, P., 1999. Detection of fluid flow variations at the Nankai trough by electric and magnetic measurements in boreholes or at the seafloor, *J. geophys. Res.,* **104,** 29 293–29 309.

Jouniaux, L., Maineult, A., Naudet, V., Pessel, M. & Sailhac, P., 2009. Review of self-potential methods in hydrogeophysics, *C. R. Geosci.,* **341**(10–11), 928–936.

Kennett, B.L.N. & Kerry, N.J., 1979. Seismic waves in a stratified half space, *Geophys. J. Int.,* **57**(3), 557–583.

Ma, J. & Plonka, G., 2010. The curvelet transform: a review of recent applications., *IEEE Signal Process. Mag.,* **27**(2), doi:10.1109/MSP.2009.935453.

Mallat, S., 1999. *A Wavelet Tour of Signal Processing,* Academic Press, New York, NY.

Mauri, G., Williams-Jones, G. & Saracco, G., 2010. Depth determinations of shallow hydrothermal system by self-potential and multi-scale wavelet tomography, *J. Volc. Geotherm. Res.,* **191,** 233–244.

Mauri, G., Williams-Jones, G., Saracco, G. & Zurek, J., 2012. A geochemical and geophysical investigation of the hydrothermal complex of Masaya volcano, Nicaragua, *J. Volc. Geotherm. Res.,* **227-228,** 15–31.

Mikhailov, O.V., Queen, J. & Toksöz, M.N., 2000. Using borehole electroseismic measurements to detect and characterize fractured (permeable) zones, *Geophysics,* **65**(4), 1098–1112.

Moon, W., Carswell, A., Tang, R. & Dillistone, C., 1986. Radon transform wave field separation for vertical seismic profiling data, *Geophysics,* **51**(4), 940–947.

Moreau, F., Gibert, D., Holschneider, M. & Saracco, G., 1997. Wavelet analysis of potential fields, *Inverse Probl.,* **13**(1), 165–178.

Murenzi, R., 1990. Ondelettes multidimensionnelles et applications à l'analyse d'images, *Doctoral Thesis,* Catholic University of Louvain, p. 217.

Pain, C., Saunders, J.H., Worthington, M.H., Singer, J.M., Stuart-Bruges, C.W., Mason, G. & Goddard, A., 2005. A mixed finite-element method for solving the poroelastic Biot equations with electrokinetic coupling, *Geophys. J. Int.,* **160,** 592–608.

Pride, S., 1994. Governing equations for the coupled electromagnetics and acoustics of porous media, *Phys. Rev.,* **50**(21), 15 678–15 696.

Pride, S. & Morgan, F.D., 1991. Electrokinetic dissipation induced by seismic waves, *Geophysics,* **56**(7), 914–925.

Pride, S.R. & Garambois, S., 2002. The role of Biot slow waves in electroseismic wave phenomena, *J. acoust. Soc. Am.,* **111**(2), 697–706, doi:10.1121/1.1436066.

Pride, S.R. & Garambois, S., 2005. Electroseismic wave theory of frenkel and more recent developments, *J. Eng. Mech.,* **131**(9), 898–907.

Rosid, M. & Kepic, A., 2005. Hydrogeological mapping using the seismoelectric method, *Explor. Geophys.,* **36**(2), 245–249.

Roueff, A., Chanussot, J. & Mars, J.I., 2006. Estimation of polarization parameters using timefrequency representations and its application to waves separation, *Signal Process.,* **86**(12), 3714–3731.

Saab, R., Wang, D., Yilmaz, O. & Herrmann, F.J., 2007. Curvelet-based primary-multiple separation from a Bayesian perspective, *SEG Expanded Abstracts,* **26,** 2510–2514, doi:10.1190/1.2792988.

Saracco, G., Moreau, F., Mathé, P., Hermitte, D. & Michel, J., 2007. Multiscale tomography of buried magnetic structures: its use in the localization and characterization of archeological structures, *Geophys. J. Int.,* **171,** 87–103.

Schakel, M. & Smeulders, D., 2010. Seismoelectric reflection and transmission at a fluid/porous-medium interface, *J. acoust. Soc. Am.,* **127**(1), 13–21, doi:10.1121/1.3263613.

Schakel, M., Smeulders, D., Slob, E. & Heller, H., 2012. Seismoelectric fluid/porous-medium interface response model and measurements, *Transp. Porous Media,* **93,** 271–282.

Schakel, M.D., Smeulders, D.M.J., Slob, E.C. & Heller, H.K.J., 2011. Seismoelectric interface response: experimental results and forward model, *Geophysics,* **76**(4), N29–N36.

Schoemaker, F.C., Grobbe, N., de Ridder, S.A.L., Slob, E.C. & Smeulders, D.M.J., 2012. Experimental validation of the electrokinetic theory and development of seismoelectric interferometry by cross-correlation, *Int. J. Geophys.,* in press.

Strahser M. H. P., 2007. Polarisation and slowness of seismoelectric signals: a case study, *Near Surf. Geophys,* **5,** 97–114, doi:10.3997/1873-0604.2006022.

Strahser, M., Jouniaux, L., Sailhac, P., Matthey, P. & Zillmer, M., 2011. Dependence of seismoelectric amplitudes on water content, *Geophys. J. Int.,* **187**(3), 1378–1392.

Thompson, A.H. & Gist, G.A., 1993. Geophysical applications of electrokinetic conversion, *The Leading Edge,* **12**(12), 1169–1173, doi:10.1190/1.1436931.

Thompson, A.H. *et al.*, 2005. Field tests of electroseismic hydrocarbon detection, *SEG Expanded Abstracts,* **24,** doi:10.1190/1.2144382, 565–568.

Thompson, A.H., Sumner, J.R. & Hornbostel, S.C., 2007. Electromagnetic-to-seismic conversion, *The Leading Edge,* **26**(4), 428–435.

Tosha, T., Matsushima, N. & Ishido, T., 2003. Zeta potential measured for an intact granite sample at temperatures to 200°C, *Geophys. Res. Lett.,* **30**(6).

Wang, D., Saab, R., Yilmaz, O. & Herrmann, F.J., 2007. Recent results in curvelet-based primary-multiple separation: application to real data, *SEG Expanded Abstracts*, **26,** 2500–2504, doi:10.1190/1.2792986.

Yarham, C. & Herrmann, F.J., 2008. Bayesian ground-roll separation by curvelet-domain sparsity promotion, *SEG Expanded Abstracts,* **27,** 2576–2580, doi:10.1190/1.3063878.

Zhang, Z.-Y., Zhang, X.-D., Yu, H.-Y. & Pan, X.-H., 2010. Noise suppression based on a fast discrete curvelet transform, *J. Geophys. Eng.,* **7**(1), 105–112.

Zheng, J., Yin, X., Zhang, G., Wu, G. & Zhang, Z., 2011. The surface wave suppression using the second generation curvelet transform, *Appl. Geophys.,* **7**(4), 325–335.

Zhu, Z., Haartsen, M.W. & Toksöz, M.N., 1999. Experimental studies of electrokinetic conversions in fluid-saturated borehole models, *Geophysics,* **64,** 1349–1356.